Appearance of half-metallicity and study of the electronic, elastics and thermodynamics properties in the Full-Heusler alloys

Y. Guermit

Thin-film physics and advanced technologies laboratory, University of Relizane, Algeria.
e-mail: gyoucef75@gmail.com

K. Hocine

Thin-film physics and advanced technologies laboratory, University of Relizane, Algeria.

Received 30 April 2025; accepted 9 March 2026

This study investigates the Full-Heusler (FH) ferromagnetic compound, Ir_2MnZ (Z=Sn, Si). We analyze the half-metallic (HM) characteristics through first-principle calculations within the density functional theory (DFT) framework. Utilizing spin-polarized computations and the full-potential linearized augmented plane-wave (FP-LAPW) approach, we employ the Generalized Gradient Approximation (GGA) and the modified Becke-Johnson (mBJ) potential. The ferromagnetic (FM) and non-magnetic (NM) phases of Cu_2MnAl- and Hg_2CuTi-type structures were investigated. The results show that the FM phase in the Cu_2MnAl-type structure is the most stable for Ir_2MnZ alloys (Z=Sn, Si). Electronic analysis reveals half-metallic ferromagnetism with integer magnetic moments of 5.0 μ_B. Mechanical parameters such as bulk modulus, shear modulus, and Poisson's ratio confirm the mechanical stability of both alloys. The half-metallic bandgaps are calculated as 0.644 eV for Ir_2MnSi and 0.23 eV for Ir_2MnSn. Thermodynamic properties, including heat capacity and Debye temperature, were evaluated using the quasi-harmonic Debye model, offering insights into the thermal stability of Ir_2MnZ. The robust HM characteristics of these compounds make them interesting candidates for spintronic devices.

Keywords: Heusler alloy; half-metallic; thermodynamic properties; FP-LAPW.

DOI: https://doi.org/10.31349/RevMexFis.72.041003

1. Introduction

Spintronics, a rapidly emerging discipline, has the potential to completely change nano-electronic systems by improving processing and memory capacity while using less energy. These devices take advantage of the spin characteristics of holes and/or electrons, which reduce the ability to interact with their orbital moments. Despite substantial advancements, semiconductor spintronics are still not as well integrated as their metallic equivalents, which are vital to magnetic memory due to magnetoresistance elements [1,2]. Since their discovery by Friedrich Heusler in 1903 [3], Heusler alloys have received substantial interest in materials science due to their wide variety of electronic, magnetic, and thermodynamic properties. These alloys are particularly valued in fields such as spintronics and magneto-electronics for their unique half-metallic ferromagnetic (HMF) nature [4], which was first identified by Groot *et al*. [5]. This property makes Heusler alloys particularly suitable for advanced technological applications, including magnetic sensors and spintronic devices [6-14]. Heusler alloys with the structural formula X_2YZ have a 2:1:1 atomic sequence, with X and Y being transition metals and Z being a main-group element (s or p group) [15-18]. These compounds can crystallize into either a Cu_2MnAl-type crystal structure with the space group $Fm\bar{3}m$ or a Hg_2CuTi-type crystal structure with the space group $F\bar{4}3m$, depending on the relationship between the X and Y atoms. In the Cu_2MnAl-type structure, X has more 3d electrons than Y, with X, Y, and Z atoms located at Wyckoff positions 8c (1/4, 1/4, 1/4), 4a (0, 0, 0), and 4b (1/2, 1/2, 1/2), respectively. Conversely, in the Hg_2CuTi-type structure, Y has more 3d electrons than X, with X atoms at positions 4a (0, 0, 0) and 4c (1/4, 1/4, 1/4), and Y and Z atoms at positions 4b (1/2, 1/2, 1/2) and 4d (3/4, 3/4, 3/4), respectively [19-23].

Iridium-based alloys have attracted attention from a large number of researchers to investigate their structural stability and the possibility of half-metallicity properties, considering their significant applications in spintronic devices, memory storage devices, tunneling magnetic resonance (TMR), and giant magnetoresistance (GMR). However, there are few experimental and theoretical studies about Ir-based Heusler alloys. Masumoto *et al*. conducted two separate experimental studies in which they measured the saturation magnetic moment and reciprocal susceptibility of Ir_2MnGa [24] and Ir_2MnAl alloys using a magnetic balance. Additionally, they determined the crystal structure of these alloys in their research. Gilleßen and Richard [25] investigated the lattice constant and magnetic moment of the Ir_2MnAl Heusler alloy through the use of density functional theory in his dissertation. Candan [26] used *ab initio* calculations to examine the electronic and magnetic properties of these alloys. Properties of the Heusler compound Ir_2MnAl, finding displayed half-metallic behaviour in GGA calculations. Ozdemir *et al*. studied structural, half-metallic and elastic properies of

Ir2MnSi. [27] predicted the structural, electronic, and magnetic properties of full Heusler alloys Ir_2YSi (Y = Sc, Ti, V, Cr, Mn, Fe, Co, and Ni) via first-principles calculations [28]. Despite extensive research on various classes of Heusler alloys, relatively few studies have focused on Iridium-based systems. Among these, Ir_2MnZ (Z = Sn, Si) stands out as an intriguing case, as it combines Iridium with Manganese and main-group elements (Sn, Si). This work aims to fill the existing gap in the literature by investigating the electronic, magnetic, elastic, and thermodynamic properties of these alloys using first-principles calculations within the DFT framework, employing the Generalized Gradient Approximation (GGA) and GGA+mBJ methods.

2. Computational details

The structural, electronic, magnetic, elastic, and thermodynamic properties of the Heusler alloys Ir_2MnSn and Ir_2MnSi were investigated using first-principles calculations based on Density Functional Theory (DFT). The calculations were carried out using the WIEN2k package [29], employing the full-potential linear augmented plane wave (FP-LAPW) method, which is well-suited for accurately capturing the electronic and structural properties of complex materials. For the exchange and correlation potentials, the Generalized Gradient Approximation (GGA) was utilized, specifically using the Perdew-Burke-Ernzerhof (PBE) parameterization [30]. Additionally, the modified Becke-Johnson (mBJ) potential was applied to improve the accuracy of the electronic structure calculations, particularly for systems with localized states [31]. The structural optimization was conducted by minimizing the total energy as a function of unit cell volume for both ferromagnetic (FM) and non-magnetic (NM) phases of Cu_2MnAl-type and Hg_2CuTi-type structures, with the equilibrium lattice constants and bulk modulus obtained from the Murnaghan equation of state [32]. The optimized structures were used for further calculations of elastic and phonon properties. The elastic constants were computed using the Irelast package developed by Murtaza *et al*. [33,34], which is integrated into the WIEN2k framework. The mechanical stability of the alloys was assessed through the analysis of elastic constants, including the bulk modulus (B), shear modulus (G), Young's modulus (E), and Poisson's ratio (ν), as well as the Zener anisotropy parameter (A) and Pugh's ratio (B/G). Phonon dispersion curves were calculated using the CASTEP code [35], which is based on density functional perturbation theory (DFPT) [36]. The phonon frequencies were evaluated using the finite displacement method, allowing for an accurate description of lattice dynamics in the high-symmetry directions of the first Brillouin zone. The computational parameters were carefully chosen to ensure the accuracy and convergence of the calculations. The muffin-tin radius (R_{mt}) was set with an $R_{mt} \cdot K_{max}$ value of 8, and a dense k-point mesh of 3000 points ($14 \times 14 \times 14$) was used for Brillouin zone integration [37].

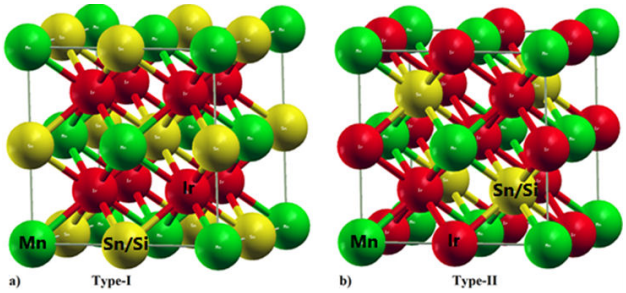

FIGURE 1. Type I (regular Heusler) and Type II (inverse Heusler) crystal structures for the Ir_2MnZ (Z = Sn, Si).

3. Results and discussion

3.1. Structural stability and mechanical properties

Determining the structural properties of a compound is a crucial step in any ab-initio study, as it enables the calculation of other important physical characteristics, such as electronic, mechanical, and thermodynamic properties. To identify the stable phases of the Ir_2MnZ (Z = Sn, Si) compounds, the total energy (E_{TOT}, in eV) as a function of unit cell volume (V, in Å^3) was calculated using the generalized gradient approximation (GGA) for the full-Heusler compounds Ir_2MnZ (Z = Sn, Si) in both the regular Cu_2MnAl-type and the inverse Hg_2CuTi-type structures, under ferromagnetic (FM) and non-magnetic (NM) states. Figures 1 illustrates the two crystal structures, Type I (regular Heusler) and Type II (inverse Heusler) for Ir_2MnSn and Ir_2MnSi. The energy versus volume curves presented in Figs. 2 and 3 emphasize the differences in stability between the two materials. Ir_2MnSi exhibits a slightly lower minimum energy in the FM Type I phase compared to Ir_2MnSn, indicating that Ir_2MnSi is thermodynamically more stable.

This greater stability is supported by its higher bulk modulus and smaller lattice constant, which contribute to a more compact and structurally robust crystal for Ir_2MnSi. The

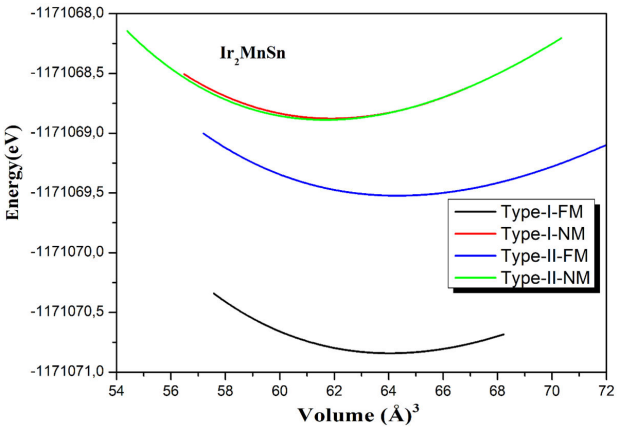

FIGURE 2. Variation of the total energy as a function of the volume of the Ir_2MnSn compound in the two types of structures: Type I (FM and NM) and Type II (FM and NM).

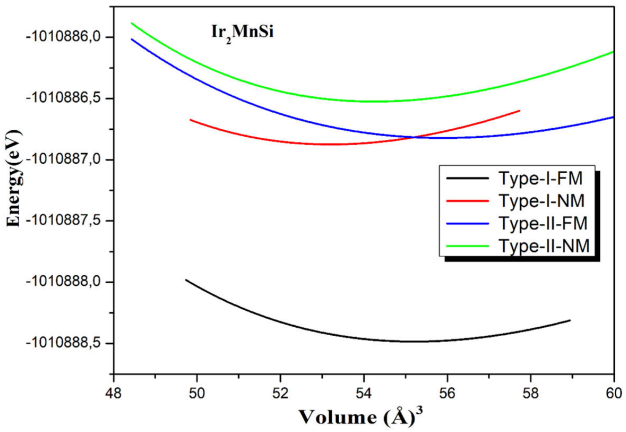

FIGURE 3. Variation of the total energy as a function of the volume of the Ir_2MnSi compound in the two types of structures: Type I (FM and NM) and Type II (FM and NM).

The structural properties of the Heusler alloys Ir_2MnSn and Ir_2MnSi were analyzed in their most stable configuration, the FM Type I phase (Cu_2MnAl-type structure), using the GGA approximation. The results presented in Fig. 2 for Ir_2MnSn and Fig. 3 for Ir_2MnSi reveal key differences in their structural parameters, which are attributed to the distinct atomic sizes and bonding strengths of Sn and Si. The lattice constant for Ir_2MnSn in the FM Type I phase is calculated to be 6.33 Å, whereas for Ir_2MnSi, it is 6.03 Å, indicating that Ir_2MnSi has a more compact structure. The relative difference in lattice constants between the two materials is approximately 4.74%, with Ir_2MnSi having the smaller lattice constant due to the smaller atomic radius of Si compared to Sn. This difference reflects the greater packing density and stronger bonding interactions present in Ir_2MnSi. In terms of mechanical properties, the bulk modulus (B) for Ir_2MnSn was calculated to be 180 GPa, while for Ir_2MnSi, it is 200 GPa, indicating that Ir_2MnSi is mechanically stiffer by approximately 10%. This increased stiffness is consistent with the smaller lattice constant of Ir_2MnSi, which leads to stronger interatomic forces and a higher resistance to compression.

The higher bulk modulus of Ir_2MnSi suggests that it is more resilient to external mechanical stresses, making it a better candidate for applications requiring high mechanical strength. Additionally, the formation energy ΔH_f for Ir_2MnSn and Ir_2MnSi, which describes their chemical stability, was calculated using the following formula:

$$\Delta H_f = E_0^{\mathrm{Ir_2MnSn/Ir_2MnSi}} - 2E_0^{\mathrm{Ir}} - E_0^{\mathrm{Mn}} - E_0^{\mathrm{Sn/Si}}, \quad (1)$$

where $E_0^{\mathrm{Ir_2MnSn/Ir_2MnSi}}$, E_0^{Ir}, E_0^{Mn} and $E_0^{\mathrm{Sn/Si}}$ are the first-principles calculated equilibrium total energies. The corresponding values are provided in Table I, and the negative values of ΔH_f [38,39], combined with the distance to the convex hull (ΔE_H) lower than 175 meV/atom [40], affirm the chemical stability of Ir_2MnSn and Ir_2MnSi, indicating their potential for experimental synthesis. Furthermore, the structural parameters detailed in Table I for the full Heusler alloys Ir_2MnZ (Z = Sn, Si) in both non-magnetic (NM) and ferromagnetic (FM) states provide critical insights into their stability and characteristics. Variations in lattice parameters and unit cell volumes across different magnetic states and structural types illustrate nuanced differences, with ferromagnetic states generally exhibiting slightly larger values. The bulk modulus, a measure of resistance to compression, typically shows higher values in non-magnetic states, reflecting greater structural rigidity. Total energy calculations reveal that ferromagnetic states exhibit lower (more negative) total energy values, indicative of enhanced stability compared to non-magnetic states. Moreover, the negative formation en-

TABLE I. The calculated structural parameters of the full Heusler alloys Ir_2MnZ (Z = Si, Sn) in non-magnetic (NM) and ferromagnetic (FM) states of Cu_2MnAl (Type-I) and Hg_2CuTi (Type-II) type structures.

Compounds	Type	Phase	a(Å)	V(Å^3)	B_0 (GPa)	B'	$\Delta E = E_{NM/FM\_\mathrm{TypeII}} - E_{FM\_\mathrm{TypeI}}$ (eV)	ΔH_0 Distance (eV/atom) [38,39]	Hull (ΔE_H) (eV/atom) [38,39]
Ir_2MnSi	Type-I	FM	**6.03**	**54.8**	**247.6**	**4.27**	**0**	-0.375	0.086
		NM	5.95	55.5	268.2	4.74	0.5973129		
	Type-II	FM	6.05	52.86	206.41	3.71	1.6633344		
		NM	5.99	53.87	262.6	4.91	1.9604264		
Ir_2MnSn	Type-I	FM	**6.33**	**63.44**	**210.0**	**4.60**	**0**	-0.161	0.083
		NM	6.26	61.33	226.94	5.12	1.955136		
	Type-II	FM	6.34	63.66	185.86	3.76	1.445612		
		NM	6.25	61.08	242.46	5.50	2.059312		
Ir_2MnSi [28]	Type-I	FM	6.03	55.01	244.44	4.623			

ergies observed for Ir_2MnSn and Ir_2MnSi underscore their chemical stability, supporting their feasibility for experimental synthesis. In comparison, Ir_2MnSi, with similar stability and desirable properties in its ferromagnetic state, provides a benchmark for evaluating these findings. Collectively, these insights highlight the robust stability of the Cu_2MnAl (Type I) structure across different Heusler alloys, laying a solid foundation for future experimental and theoretical investigations.

The study of elastic properties is crucial for understanding the mechanical and dynamic behavior of materials, as it provides valuable insights into the internal forces acting within solids. Elastic constants are particularly important as they connect mechanical deformations with the material's response to applied stress, revealing the stiffness and bonding strength within the crystal lattice. The phonon characteristics discussed earlier are directly linked to these elastic properties, as vibrational modes are influenced by the crystal's stiffness, quantified by the elastic constants. When a crystal undergoes stress, it deforms, leading to changes in its defining parameters, referred to as homogeneous deformations. Near equilibrium, the energy can be approximated by a quadratic function, leading to the linear relationship described by Hooke's law between stress and strain. This relationship is characterized by elastic constants, which are also essential for determining the mechanical stability of the crystal. For stability, the quadratic form of energy must be positive definite, imposing specific constraints on the elastic constants. Elastic constants, therefore, measure a crystal's resistance to external forces, and methods such as volume conservation or stress-strain techniques are typically used to determine them [41,42]. In this study, we employed the volume conservation technique to calculate the specific elastic constants C_{11}, C_{12}, and C_{44} for the cubic system of Ir_2MnZ (Z = Sn, Si). From these constants, additional elastic properties, including shear modulus (G), Young's modulus (E), and Poisson's ratio (ν), were derived using the following equations [43-47]:

$$E = \frac{9BG}{3B+G}, \tag{2}$$

$$G = \frac{C_{11} - C_{12} + 3C_{44}}{5}, \tag{3}$$

$$B = \frac{C_{11} + 2C_{12}}{3}, \tag{4}$$

$$\nu = \frac{3B - 2G}{2(3B+G)}, \tag{5}$$

$$A = \frac{2C_{44} + C_{12}}{C_{11}}, \tag{6}$$

To ensure mechanical stability, the conditions C_{11}, C_{44}, $C_{11} - C_{12}$, and $C_{11} + 2C_{12} > 0$ must be satisfied. Additionally, the condition $C_{12} < B < C_{11}$ must hold [48]. As shown in Table II, both Ir_2MnSn and Ir_2MnSi in the regular Heusler Type I (Cu_2MnAl-type) structure meet these stability criteria.

The bulk modulus (B_0) quantifies a material's resistance to compression, with higher values indicating stronger resistance to volume change. According to the data in Table II, the calculated G values confirm that both Ir_2MnSn and Ir_2MnSi are relatively hard materials. The stiffness of the materials, predicted by Young's modulus (E), shows that higher E values correspond to greater stiffness. The elastic constant C_{11}, which reflects the material's resistance to unidirectional compression along primary crystallographic axes, is lower than C_{44}, which measures resistance to shear deformation. This

TABLE II. Values of the anisotropy parameter A, the elastic constants C_{ij} (GPa), the shear modulus G (GPa), the Young's modulus E (GPa), elastic wave velocities termed as transverse v_t (m.s^{-1}), longitudinal velocities v_l (m.s^{-1}), average wave velocity v_m (m.s^{-1}) for the compounds Ir_2MnSn and Ir_2MnSi.

Compounds	Ir_2MnSi	Ir_2MnSn
B	247.47(247.61) 140.85(244.445) [28]	200.84(210.08)
C_11	273.24 124.31 [28]	214.35
C_12	234.41149.13 [28]	194.49
C_44	205.84 75.42 [28]	378.91
G	131.27 40.29 [28]	231.31
B/G	1.88	0.86
E	334.46	501.44
A	10.6	4.442
ν	0.27	0.038
vs	3389.0	4053.25
vl	5460.46	6014.14
vm	3389.0	4424.25

TABLE III. The gap energy (E_g) obtained by the GGA and GGA+mBJ approximation.

Compound	Gap energy E_g (eV) - GGA	Gap energy E_g (eV) - GGA+mBJ
Ir_2MnSi	0.556	0.644
Ir_2MnSn	0	0.23
Ir_2MnSi [28]	0.55	-

indicates that Ir_2MnSi exhibits stronger resistance to unidirectional compression, while Ir_2MnSn shows greater resistance to shear deformation. To quantify the elastic anisotropy of these compounds, we calculated the anisotropy factor A using the values of the elastic constants. Elastic anisotropy is crucial in engineering applications, as it indicates that a material's properties vary with direction. An anisotropic material exhibits different mechanical characteristics depending on its orientation. According to Table II, the anisotropy factors for Ir_2MnSn and Ir_2MnSi are 4.442 and 10.6, respectively. Since an isotropic crystal has an A value of 1, both materials demonstrate significant elastic anisotropy, with Ir_2MnSi being more anisotropic. Pugh's criterion [49] offers an empirical relationship linking the plastic properties of a material with its elasticity. The ratio B/G is a useful metric to predict whether a material behaves in a ductile or brittle manner. A B/G ratio higher than 1.75 indicates ductility, while a lower value indicates brittleness. In our case, B/G values of 0.86 for Ir_2MnSn and 1.81 for Ir_2MnSi indicate that Ir_2MnSn is brittle, while Ir_2MnSi behaves in a ductile manner. Additionally, Poisson's ratio (ν), which characterizes the lateral contraction of a material when subjected to a longitudinal strain, was calculated as 0.038 for Ir_2MnSn and 0.27 for Ir_2MnSi. Since materials with $\nu > 0.26$ are considered ductile, these results confirm that Ir_2MnSi is ductile in nature.

Another parameter used to assess the ductility or brittleness of a material is the Cauchy pressure [50]. We also calculated the average sound velocity in the polycrystalline material using the following formula [51]:

$$v_m = \left[\frac{1}{3}\left(\frac{2}{v_t^3} + \frac{1}{v_l^3}\right)\right]^{1/3}, \tag{7}$$

where v_l and v_t are, respectively, the longitudinal and transverse sound velocities obtained using the shear modulus G and the bulk modulus B from Navier's equation [52]:

$$v_l = \left(\frac{3B + G}{3\rho}\right)^{1/2}, \tag{8}$$

$$v_t = \left(\frac{G}{\rho}\right)^{1/2}, \tag{9}$$

The calculated sound velocities for Ir_2MnSi and Ir_2MnSn in the Cu_2MnAl (Type-I) structure are listed in Table II. To the best of our knowledge, the elastic constants and related

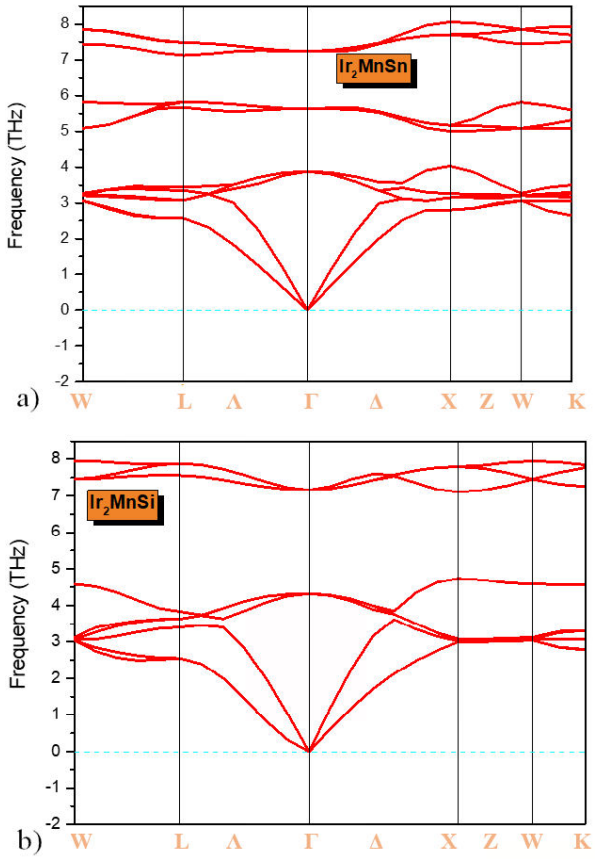

FIGURE 4. Phonon dispersion analysis of Ir_2MnSn and Ir_2MnSi compounds

properties for Ir_2MnSn have not been previously reported. For Ir_2MnSi, our results show a notable difference compared to those of Özdemir *et al*. [27]. This discrepancy can be attributed to the fact that our elastic property calculations were performed under the same conditions as the structural properties, particularly with $B_0^{\text{structural}} = B_0^{\text{elastic}}$ (see Table III). We hope our calculations will help to fill the gap in the existing data for these compounds.

In addition to energy and elastic results, an in-depth analysis of the phonon spectra (Fig. 4) provides key insights into the atomic dynamics and mechanical stability of these materials. The phonon spectra reveal a total of 12 branches, comprising 3 acoustic branches (one longitudinal acoustic and two transverse acoustic modes) and 9 optical branches (transverse optical [TO] and longitudinal optical [LO] modes). The phonon spectra of Ir_2MnSn and Ir_2MnSi (Fig. 4) display notable differences between the acoustic and optical modes, reflecting disparities in atomic mass and bonding characteristics.

For Ir_2MnSi, the gap between the acoustic and transverse optical branches is relatively narrow, indicating that the vibrational frequencies of these modes are quite similar. This is due to comparable atomic masses and bonding strengths between Mn and Si atoms in the lattice. Conversely, in Ir_2MnSn, the gap between the acoustic and optical branches

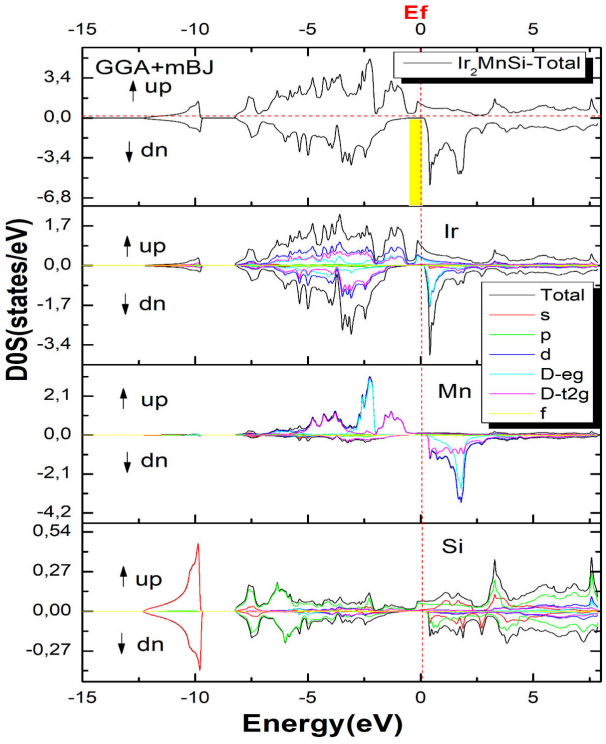

FIGURE 5. Observed total densities of states (DOS) and partial densities of states (PDOS) of Ir_2MnSn compound.

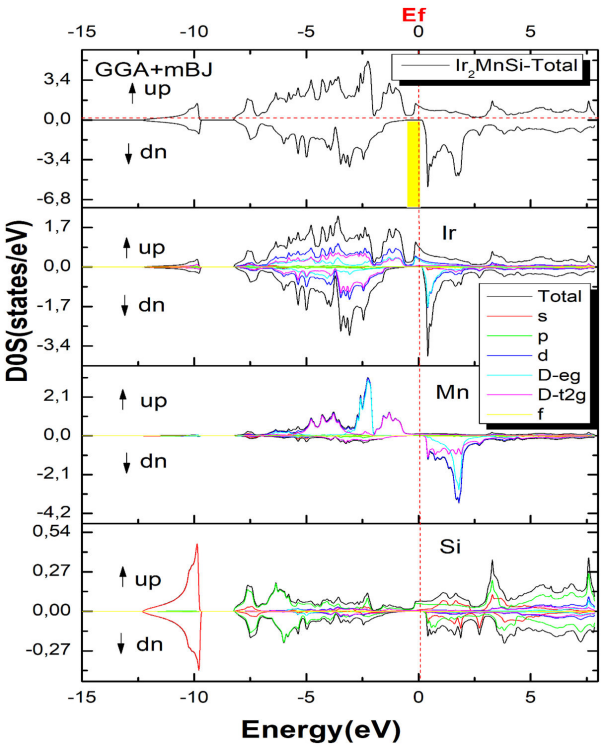

FIGURE 6. Observed total densities of states (DOS) and partial densities of states (PDOS) of Ir_2MnSi compound.

is more pronounced, suggesting more distinct vibrational interactions between the modes. Additionally, in Ir_2MnSi, a significant gap between the transverse and longitudinal optical branches indicates that the bonds responsible for longitudinal vibrations are stiffer, resulting in higher frequencies for the LO modes. In contrast, Ir_2MnSn shows a smaller gap between these optical branches, reflecting a more uniform bonding environment around Mn, leading to less disparity in bond stiffness affecting the transverse and longitudinal optical modes. These differences in phonon spectra directly influence the thermal and mechanical properties of the alloys. The larger gap between the acoustic and optical branches in Ir_2MnSn suggests that the phonon contribution to thermal conductivity (k_L) is lower, making this alloy more suitable for thermoelectric applications, where reduced thermal conductivity is essential for improved energy efficiency. Specifically, the smaller gap between the TO and LO branches in Ir_2MnSn implies more efficient phonon scattering, further lowering k_L and enhancing thermal performance for applications requiring efficient thermal insulation. In contrast, Ir_2MnSi, with its stiffer longitudinal bonds (evidenced by the larger gap between TO and LO modes), shows superior mechanical and thermal stability at elevated temperatures. This is supported by the shear modulus (G) and Young's modulus (E), which indicate that this alloy offers greater resistance to mechanical deformations. Moreover, the Poisson's ratio (ν) and B/G ratio confirm that Ir_2MnSi behaves more ductilely, making it an ideal candidate for applications where mechanical resilience is critical. While Ir_2MnSn stands out due to its lower thermal conductivity, favoring thermoelectric applications, Ir_2MnSi is better suited for high-temperature environments thanks to its superior mechanical stability and stiffer bonds, as evidenced by the phonon spectra. These findings, illustrated by the phonon dispersion figures (Figs. 4, 5, and 6), demonstrate the importance of examining phonon dynamics in designing materials tailored for specific thermal and mechanical applications.

3.2. Electronic and magnetic properties

The electronic and magnetic properties of Ir_2MnSn and Ir_2MnSi were analyzed using density of states (DOS) calculations, as illustrated in Figs. 5 and 6. These DOS plots reveal the contributions of the different atomic states (Ir, Mn, Sn, Si) to the overall electronic structure, providing deeper insights into the materials' half-metallic nature.

In both compounds, the majority spin channel exhibits metallic behavior, with states crossing the Fermi level (E_F), while the minority spin channel presents a semiconducting gap. This feature is characteristic of half-metallicity, where one spin channel is conductive, and the other is insulating. The Mn/d-states are the dominant contributors to the magnetic and electronic properties in both compounds. In Ir_2MnSi, the strong exchange splitting between the spin-up and spin-down Mn d-states leads to the formation of a larger minority spin gap (0.644 eV), compared to Ir_2MnSn, where the gap is smaller (0.23 eV), as shown in Figs. 7 and 8. This difference is due to the stronger bonding and smaller atomic radius of Si, which enhances the overlap between CMn and

TABLE IV. Total and partial magnetic moment in unit of μ_B for Ir_2MnSn and Ir_2MnSi.

Compounds	Method	Ir (μ_B)	Mn (μ_B)	Sn/Si (μ_B)	Interstitial (μ_B)	Total magnetic moment (μ_B)
Ir_2MnSn	GGA-mbj	0.54	3.93	-0.004	-0.02	5.00
Ir_2MnSi		0.605	3.767	0.018	0.0029	5.00
	GGA	0.598	3.66	0.030	0.111	5.00
Ir_2MnSi [28]		0.573	3.558	-	-	5.00

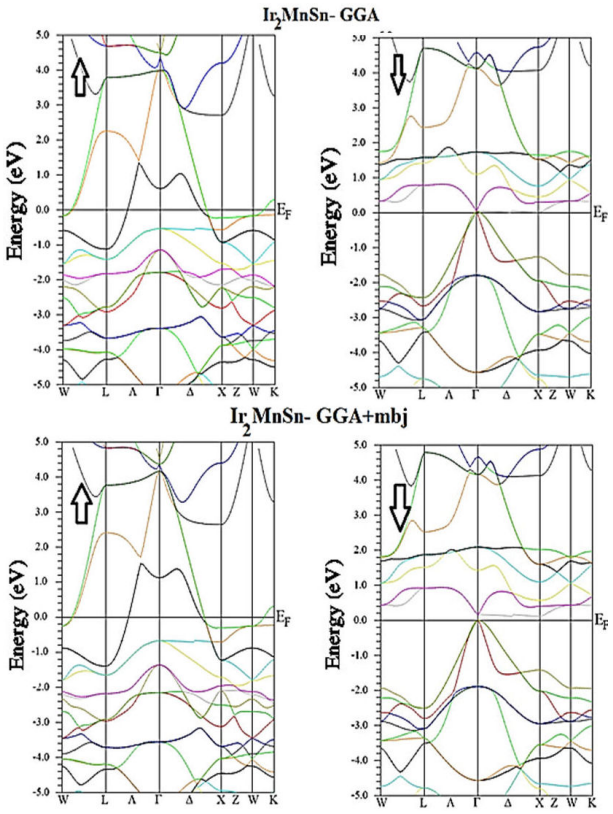

FIGURE 7. The band structure of spin-up and spin-dn electrons for Ir_2MnSn in both GGA and GGA-mBJ approximations.

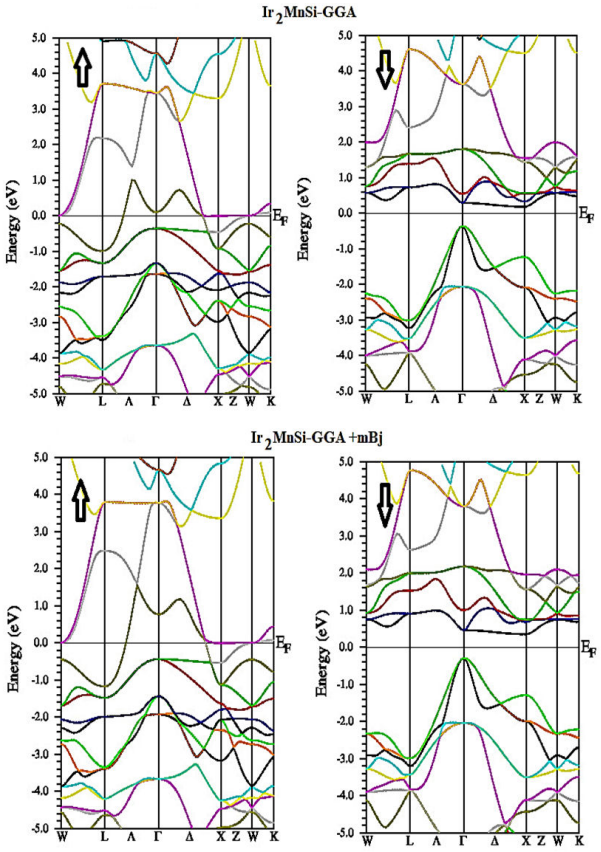

FIGURE 8. The band structure of spin-up and spin-dn electrons for Ir_2MnSi in both GGA and GGA-mBJ approximations.

Si orbitals, leading to a more pronounced splitting of the Mn/d-states. The larger gap in the minority spin channel of Ir_2MnSi ensures that it retains its half-metallic properties more robustly, even at elevated temperatures, making it an ideal candidate for spintronic applications. In Ir_2MnSn, although the Mn d-states still play a key role, the weaker interaction with Sn results in a smaller gap in the minority spin channel, reducing the robustness of its half-metallicity compared to Ir_2MnSi. However, Ir_2MnSn still displays significant half-metallic behavior, as shown by the clear separation between the metallic majority spin channel and the gapped minority spin channel. The Ir/d-states also contribute to the DOS, particularly around the Fermi level in the majority spin channel, but their contribution is smaller compared to the Mn atoms. In both materials, the Ir d-states hybridize with the Mn d-states, particularly in the majority spin channel, which enhances the metallic character. In the minority spin channel, the Ir d-states are largely suppressed, contributing to the formation of the semiconducting gap. This suppression further supports the half-metallic behavior by maintaining the gap in the minority spin channel. For the non-magnetic elements, Sn and Si, their contributions are primarily found at lower energies, away from the Fermi level. Si exhibits stronger interactions with Mn due to its smaller size and higher electronegativity, which contributes to the larger band gap in the minority spin channel for Ir_2MnSi. In contrast, Sn has a more limited impact on the electronic structure near the Fermi level, leading to the smaller band gap observed in Ir_2MnSn. The total magnetic moments for both compounds were calculated to be approximately 5.00 μ_B per formula unit, following the Slater-Pauling rule [53], as shown in Table IV.

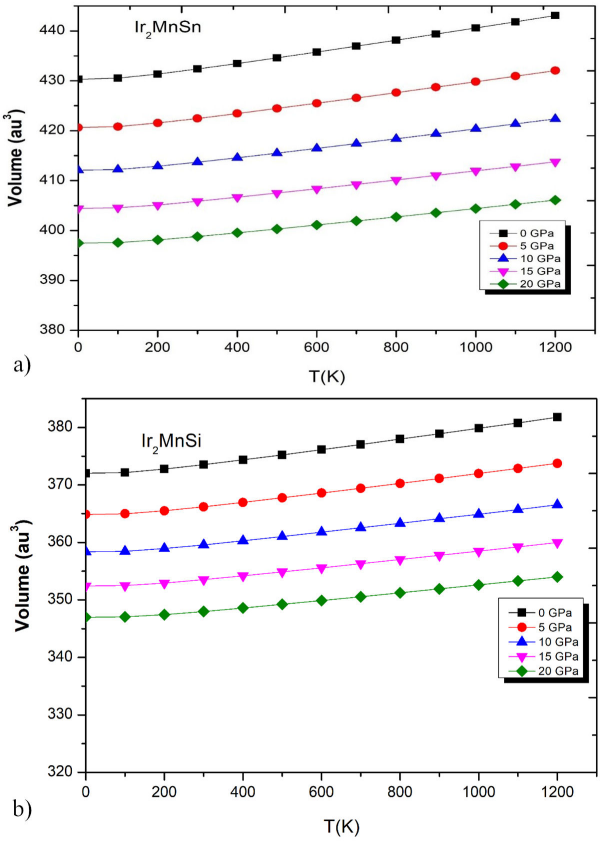

FIGURE 9. Volume variation as a function of temperature at different pressures for full- Heusler alloys Ir_2MnZ (Z = Sn, Si).

The majority of the magnetic moment is contributed by the Mn atoms, with the Mn atoms in Ir_2MnSi exhibiting a magnetic moment of 3.40 μ_B, slightly higher than the 3.29 μ_B observed for Ir_2MnSn. This difference can be attributed to the stronger exchange splitting in Ir_2MnSi, which is a result of its stronger Mn-Si bonding. The Ir atoms contribute a smaller antiparallel magnetic moment of approximately -0.13 μ_B for both materials, slightly reducing the total magnetization. The Sn and Si atoms, being non-magnetic, contribute negligibly to the total moment. The difference in magnetic moments between Ir_2MnSi and Ir_2MnSn is primarily due to the stronger Mn-Si interaction in Ir_2MnSi, which leads to a slightly higher magnetic moment in this compound. The total magnetic moment of both compounds is largely determined by the Mn/d-states, whose strong exchange splitting is responsible for the formation of the gap in the minority spin channel. The overall magnetic properties of these materials, combined with their electronic structure, confirm their potential as half-metallic ferromagnets, particularly in the case of Ir_2MnSi, where the larger minority spin gap and stronger magnetic interactions make it a more robust candidate for spintronic applications. The strong half-metallic nature of Ir_2MnSi makes it a prime candidate for spintronic applications, particularly because the large minority spin gap ensures high spin polarization at the Fermi level, even at elevated temperatures. This high degree of spin polarization is critical for devices like magnetic tunnel junctions and spin valves, where efficient spin injection is required. Ir_2MnSn also exhibits half-metallicity, though its smaller gap makes it slightly less ideal for high-temperature applications. However, both materials show great promise for use in spintronic devices due to their robust magnetic moments and high spin polarization.

3.3. Thermodynamic properties

The thermodynamic properties of Ir_2MnSn and Ir_2MnSi were analyzed as a function of temperature and pressure. The following figures illustrate variations in volume, heat capacity, thermal expansion coefficient, and Debye temperature for both materials. A comparison between the two alloys highlights their distinct thermodynamic behaviors. Figure 9 shows the variation of volume as a function of temperature at different pressures for both alloys. Both materials exhibit an increase in volume with rising temperature, which is typical for solids. However, Ir_2MnSi shows a slightly smaller volume variation than Ir_2MnSn at all pressures, suggesting that Ir_2MnSi is more thermally stable and more resistant to thermal expansion. This difference can be attributed to the more compact nature of Mn-Si bonds, which enhance the stability of the crystal lattice compared to Mn-Sn. This indicates that at high temperatures, Ir_2MnSi is better able to maintain its structure and resist thermal deformations, an important factor for high-temperature applications. Figure 10 illustrates the variation of heat capacity at constant volume (C_v) as a function of temperature at different pressures. The heat ca-

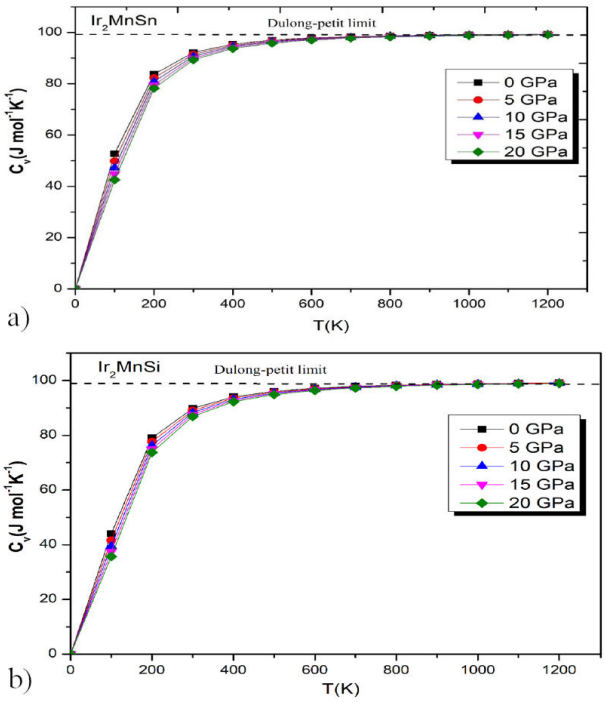

FIGURE 10. The variation of the heat capacity C_v as a function of temperature at different pressures for full-Heusler alloys Ir_2MnZ (Z = Sn, Si).

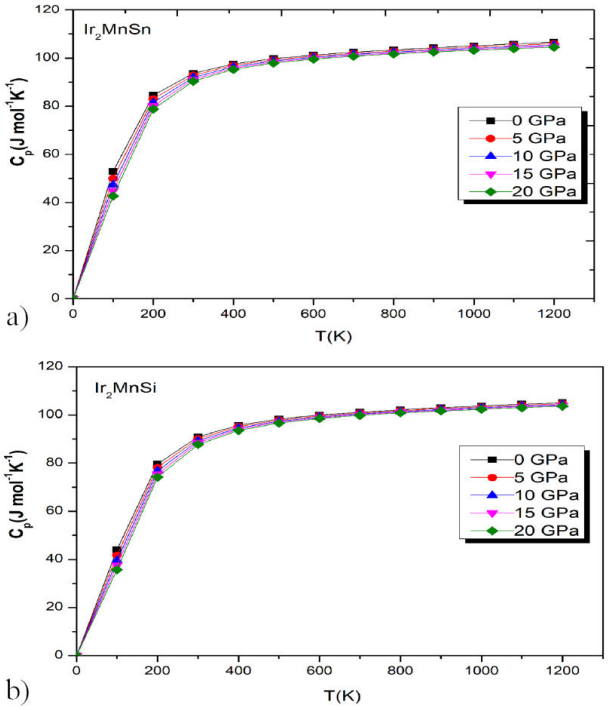

FIGURE 11. The variation of the heat capacity Cp as a function of temperature at different pressures for full-Heusler alloys Ir_2MnZ (Z=Sn,Si).

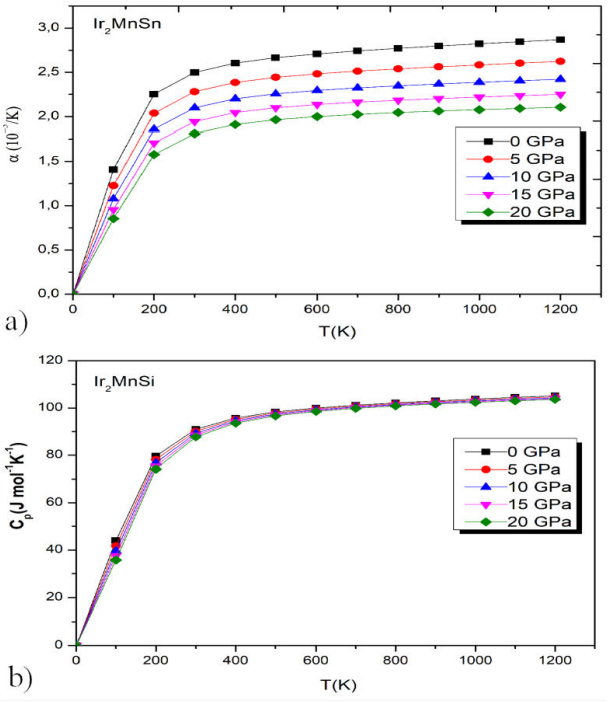

FIGURE 12. The thermal expansion coefficient α as a function of temperature at different pressures for full-Heusler alloys Ir_2MnZ (Z = Sn, Si).

pacity increases with temperature for both materials. However, Ir_2MnSi shows slightly higher C_v values than Ir_2MnSn, especially at higher temperatures. This difference suggests

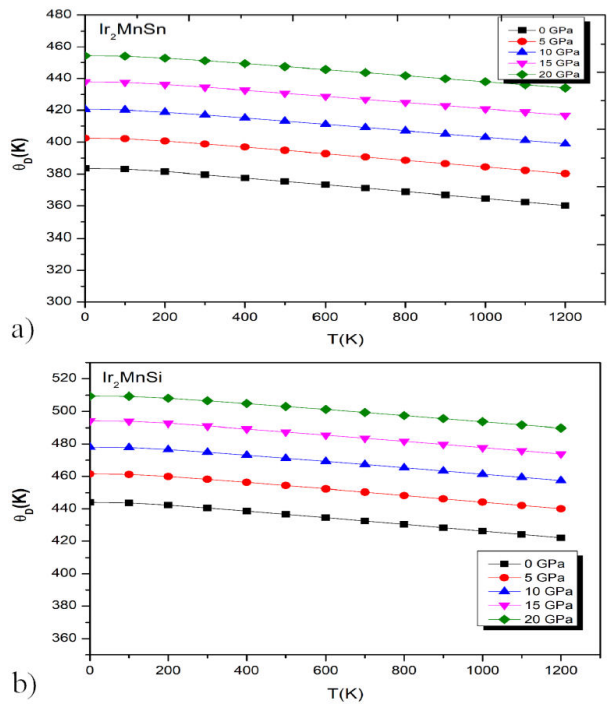

FIGURE 13. The variation of the Debye temperature as a function of temperature at different pressures for full-Heusler alloys Ir_2MnZ (Z = Sn, Si).

that Ir_2MnSi has a greater capacity to absorb heat without experiencing rapid temperature increases. This may be related to its more stable crystal structure and stronger interactions between Mn and Si, which promote better internal thermal energy management. Figure 11 shows the heat capacity at constant pressure (C_p) for both alloys as a function of temperature. Similar to heat capacity at constant volume, Ir_2MnSi shows higher C_p values than Ir_2MnSn. These results reinforce the idea that Ir_2MnSi has a greater capacity to dissipate heat without experiencing rapid temperature increases, making it potentially more effective in thermally demanding environments. Figure 12 presents the variation of the thermal expansion coefficient (α) as a function of temperature. Both materials show an increase in α with temperature, indicating increased thermal expansion as the temperature rises. However, Ir_2MnSi exhibits a lower thermal expansion coefficient than Ir_2MnSn at all temperatures and pressures. This means that Ir_2MnSi is less susceptible to thermal expansion, further reinforcing its high-temperature stability. This property makes Ir_2MnSi more suitable for applications where minimal thermal expansion is required to maintain structural integrity. Figure 13 shows the Debye temperature for both materials as a function of temperature at different pressures. The Debye temperature is a key indicator of a material's stiffness and its ability to resist thermal vibrations. Ir_2MnSi exhibits higher Debye temperatures than Ir_2MnSn (440 K), reflecting greater stiffness and stronger resistance to atomic vibrations. A material with a higher Debye temperature, like Ir_2MnSi (380 K), is more resistant to thermal disturbances, which gives it superior mechanical and thermal stability at elevated temper-

atures. Overall, the comparison of thermodynamic properties between Ir_2MnSn and Ir_2MnSi shows that Ir_2MnSi is the more thermodynamically stable alloy. Ir_2MnSi exhibits less volume variation, higher heat capacity, and a lower thermal expansion coefficient, making it better suited for high-temperature environments. The higher Debye temperature of Ir_2MnSi also confirms its superior mechanical and thermal resistance. In contrast, Ir_2MnSn is slightly less thermally stable, with a stronger response to temperature and pressure variations, making it less suitable for applications requiring high thermal stability.

4. Conclusions

In this work we investigate Ir_2MnZ (Z = Sn, Si) full-Heusler compound with Density Functional Theory (DFT) with PBE-GGA and GGA-mBJ exchange correlation function utilizing full potential augmented plan wave (FP-LAPW), provided a comprehensive understanding of its properties in several domains. Additionally, Ir_2MnZ (Z = Sn, Si) were identified as a half-metallic Heusler alloy. In the spin-down state, it exhibited an indirect bandgap semiconductor behavior with an energy of 0.556 eV and 0 eV for Ir_2MnSi and Ir_2MnSn with GGA, respectively, and 0.644 eV and 0.23 eV, as determined using GGA-mBJ. Conversely, in the spin-up state, the compounds displayed metallic behavior. The above analysis has been confirmed by the examination of the electrical band structure and density of states (DOS). The elastic properties further validate the structural stability of both alloys in the studied phase. According to Pugh's criteria, Ir_2MnSn is classified as brittle, while Ir_2MnSi exhibits a more ductile nature, highlighting their differing mechanical behaviors. Magnetic calculations show that both alloys exhibit a total magnetic moment of approximately $5\mu_B$, largely attributed to the Mn atoms, which play a significant role in determining their overall magnetic characteristics. Finally, key thermodynamic parameters such as lattice constants, thermal expansion coefficients, heat capacities, and Debye temperatures were determined across a pressure range from 0 to 20 GPa for both alloys. The Debye temperature results, in particular, correlate with the elastic constants, indicating that Ir_2MnSi, with its greater rigidity and thermal stability, is more suitable for applications requiring enhanced performance under varying thermal and mechanical conditions. Finally, this study offers a thorough analysis of the diverse properties of Heusler alloys Ir_2MnZ (Z = Sn, Si):

- Structural stability and compatibility: They generally exhibit high chemical and thermodynamic stability, and they have excellent lattice matching with conventional materials.
- Tunable properties: Their electronic and magnetic properties can be adjusted by changing the atomic ordering or through doping (valence electron count).
- High magnetic moments: Many possess high magnetic moments.

Due to these properties, these studied compounds have promising potential in developing spin-electronics.

1. G. H. F. Felser, Claudia and B. Balke, Spintronics: a challenge for materials science and solid-state chemistry, *Angewandte Chemie International Edition* **46** (2007) 668, https://doi.org/10.1002/anie.200601815
2. T. Heusler, F., The nature of the Heusler alloys. *Transactions of the Faraday Society* **08** (1912) 169, https://doi.org/10.1039/TF9120800169
3. I. Galanakis, P. H. Dederichs, and N. J. P. R. B. Papanikolaou, Origin and properties of the gap in the half-ferromagnetic Heusler alloys, *Physical Review B* **66** (2002) 134428, https://doi.org/10.1103/PhysRevB.66.134428
4. M. Halder *et al*., Revealing the nature of magnetic phases in the semi-Heusler alloy Cu0.85Ni0.15MnSb, *Journal of Magnetism and Magnetic Materials* **374** (2015) 75, https://doi.org/10.1016/j.jmmm.2014.08.061.
5. R. A. D. Groot *et al*., New class of materials: half-metallic ferromagnets, *Physical Review Letters* **50** (1983) 2024, https://doi.org/10.1103/PhysRevLett.50.2024.
6. Y. Guermit *et al*., Phase stability, electronic, magnetic and elastic properties of Ni2CoZ (Z= Ga, Sn): A first principles study with GGA method and GGA+U approach, *Chinese Journal of Physics* **56** (2018) 1394, https://doi.org/10.1016/j.cjph.2018.05.015
7. M. Drief *et al*., First-Principle Study of Half-Metallic Ferrimagnet Behavior in Titanium-Based Heusler Alloys Ti2FeZ (Z= Al, Ga, and In), *Journal of Superconductivity and Novel Magnetism* **31** (2018) 1059, https://doi.org/10.1103/PhysRevB.66.134428.
8. I. Zuti'c, J. Fabian, and S. D. Sarma, Spintronics: Fundamentals and applications, *Reviews of Modern Physics* **76** (2004) 323, https://doi.org/10.1103/RevModPhys.76.323
9. A. Candan *et al*., Electronic structure and vibrational properties in cobalt-based full-Heusler compounds: A first principle study of Co2MnX (X = Si, Ge, Al, Ga), *Journal of Alloys and Compounds* **560** (2013) 215, https://doi.org/10.1016/j.jallcom.2013.01.102
10. S. Khmelevskyi *et al.*, Microscopic origin of ferroantiferromagnetic transition upon non-magnetic substitution in Ru2(Mn1-xVx)Ge full Heusler alloys, *Journal of Alloys and Compounds* **692** (2017) 178, https://doi.org/10.1016/j.jallcom.2016.09.017
11. X.-P. Wei *et al.*, Investigations on full-Heusler alloys Mn2TaAl and Mn2WAl for spintronic and thermoelectric applications, *iScience* **27** (2024), https://www.cell.com/iscience/fulltext/S2589-0042(24)02482-9

12. X.-P. Wei *et al.*, Investigations on stability, Gilbert damping, electronic and magnetic properties along with Curie temperature for quaternary Heusler alloys CrTiCoZ, *Results in Physics* **58** (2024) 107512, https://doi.org/10.1016/j.rinp.2024.107512

13. X.-P.Wei *et al*., Gilbert damping, electronic and magnetic properties for quaternary Heusler alloys CrYCoZ: First-principles and Monte Carlo studies, *Computational Materials Science* **210** (2022) 111453, https://doi.org/10.1016/j.commatsci.2022.111453

14. X. Zhang *et al*., Half-metallic quaternary CrYCoX (X= Si, Ge, Sn, Pb) alloys: DFT calculations and Monte Carlo simulation, *Materials Today Communications* **33** (2022) 104650, https://doi.org/10.1016/j.mtcomm.2022.104650

15. Y. Guermit *et al*., Theoretical investigation of magnetic, electronic, thermoelectric and thermodynamic properties of Fe2TaZ (Z= B, In) compounds by GGA and GGA+U approaches, *Computational Condensed Matter* **22** (2020) e00438, https://doi.org/10.1016/j.cocom.2019.e00438

16. Y. Guermit *et al.*, Investigation of structural, elastic, electronic, magnetic and thermoelectric proprieties for Mn2RhZ (Z= Al, Si and Ge) full-Heusler alloys, *International Journal of Thermophysics* **42** (2021) 1, https://doi.org/10.1007/s10765-020-02751-0.

17. K. Hocine *et al*., Structural, electronic and optical properties of the Half-Heusler MgYGa alloy Via DFT calculations, *Revista Mexicana de Física* **70** (2024) 030502, https://doi.org/10.31349/RevMexFis.70.030502

18. N. Xing *et al.*, First-principle prediction of half-metallic properties for the Heusler alloys V2YSb (Y= Cr, Mn, Fe, Co), *Computational Materials Science* **45** (2009) 489, https://doi.org/10.1016/j.commatsci.2008.12.001.

19. N. Kervan and S. Kervan, A first-principle study of halfmetallic ferrimagnetism in the Ti2CoGa Heusler compound, *Journal of Magnetism and Magnetic Materials* **324** (2012) 645, https://doi.org/10.1016/j.jmmm.2011.09.047.

20. Y. Gupta, M. M. Sinha, and S. S. Verma, Lattice dynamics of novel Heusler alloys MnY2Z (Z= Al and Si), *Physica B: Condensed Matter* **590** (2020) 412222, https://doi.org/10.1016/j.physb.2020.412222.

21. Y. Gupta, M. M. Sinha, and S. S. Verma, Effect of spinpolarization on structural, electronic, and lattice dynamical properties of "MnY2Ga" full Heusler alloy, *Physica B: Condensed Matter* **624** (2022) 413425, https://doi.org/10.1016/j.physb.2021.413425

22. Y. Gupta, M. M. Sinha, and S. S. Verma, Exploring the structural, elastic, lattice dynamical stability and thermoelectric properties of semiconducting novel quaternary Heusler alloy LiScPdPb, *Journal of Solid State Chemistry* **304** (2021) 122601, https://doi.org/10.1016/j.jssc.2021.122601

23. Y. Gupta, M. M. Sinha, and S. S. Verma, First-principles investigation on the electronic, mechanical and lattice dynamical properties of novel AlNiX (X= As and Sb) half-Heusler alloys, *Materials Today Communications* **26** (2021) 101885, https://doi.org/10.1016/j.mtcomm.2020.101885.

24. H. Masumoto, K. Watanabe, and S. Ohnuma, New Compounds of the Clb, Cl Types of IrMnSb and PdMnTe, New L21 (Heusler) Type of Ir2MnGa Alloys, and Magnetic Properties, *Journal of the Physical Society of Japan* **32** (1972) 570, https://doi.org/10.1143/JPSJ.32.570

25. M. Gilleßen and R. Dronskowski, Maßgeschneidertes und Analytik-Ersatz: über die quantenchemischen Untersuchungen einiger ternärer intermetallischer Verbindungen, Tech. Rep. RWTH-CONV-113777, Fachgruppe Chemie, RWTH Aachen (2010), https://publications.rwth-aachen.de/record/51488.

26. A. Candan, A study on magnetic, electronic, elastic and vibrational properties of Ir2MnAl Heusler alloy for spintronic applications, *Materials Research Express* **6** (2019) 096571, https://doi.org/10.1088/2053-1591/ab2f9b.

27. E. G. Ozdemir, E. R. H. A. N. Eser, and Z. Y. A. Merdan, Investigation of structural, half-metallic and elastic properties of a new full-Heusler compound-Ir2MnSi, *Chinese Journal of Physics* **56** (2018) 1551, https://doi.org/10.1016/j.cjph.2018.03.021.

28. R. Prakash and G. Kalpana, Prediction of structural, electronic and magnetic properties of full Heusler alloys Ir2YSi (Y= Sc, Ti, V, Cr, Mn, Fe, Co, and Ni) via first-principles calculation, *AIP Advances* **11** (2021), https://doi.org/10.1063/5.0038405.

29. P. Blaha et al., wien2k: An augmented plane wave+ local orbitals program for calculating crystal properties, *Computational Physics Communications* **60** (2001), http://www.wien2k.at/reg_user/textbooks/usersguide.pdf

30. J. P. Perdew, K. Burke, and M. Ernzerhof, Generalized Gradient Approximation Made Simple, *Physical Review Letters* **77** (1996) 3865, https://doi.org/10.1103/PhysRevLett.77.3865

31. F. Tran and P. Blaha, Accurate Band Gaps of Semiconductors and Insulators with a Modified Becke-Johnson Exchange Potential, *Physical Review Letters* **102** (2009) 226401, https://doi.org/10.1103/PhysRevLett.102.226401

32. F. D. Murnaghan, The Compressibility of Media under Extreme Pressures, *Proceedings of the National Academy of Sciences* **30** (1944) 244, https://doi.org/10.1073/pnas.30.9.244.

33. M. Jamal, *et al*., IRelast package, *J. Alloys Compd.* **735** (2018) 569, https://doi.org/10.1016/j.jallcom.2017.10.139

34. A. Boochani, Co2CrAl heuslerene: Mechanical, thermodynamic and electronic properties, Metals **13** (2023) 582, https://www.mdpi.com/2075-4701/13/3/582

35. M. D. Segall *et al.*, First-principles simulation: ideas, illustrations and the CASTEP code, Journal of Physics: Condensed Matter **14** (2002) 2717, https://iopscience.iop.org/article/10.1088/0953-8984/14/11/301/meta

36. S. Baroni *et al.*, Phonons and related crystal properties from density-functional perturbation theory, *Rev. Mod. Phys.* **73** (2001) 515, https://doi.org/10.1103/RevModPhys.73.515.

37. H. J. Monkhorst and J. D. Pack, Special points for Brillouin-zone integrations, *Physical Review B* **13** (1976) 5188, https://doi.org/10.1103/PhysRevB.13.5188

38. J. E. Saal *et al*., Materials design and discovery with high-throughput density functional theory: the open quantum materials database (OQMD), *Jom* **65** (2013) 1501, https://link.springer.com/article/10.1007/S11837-013-0755-4

39. S. Kirklin *et al.*, The Open Quantum Materials Database (OQMD): assessing the accuracy of DFT formation energies, *npj Computational Materials* **1** (2015) 1, https://www.nature.com/articles/npjcompumats201510

40. N. M. Fortunato *et al*., High-throughput design of all-d-metal Heusler alloys for magnetocaloric applications, arXiv preprint arXiv:2306.17092 (2023), https://arxiv.org/abs/2306.17092

41. O. H. Nielsen and R. M. Martin, First-principles calculation of stress, *Physical Review Letters* **50** (1983) 697, https://doi.org/10.1103/PhysRevLett.50.697

42. Y. L. Page and P. Saxe, Symmetry-general least-squares extraction of elastic data for strained materials from ab initio calculations of stress, *Physical Review B* **65** (2002) 104104, https://doi.org/10.1103/PhysRevB.65.104104

43. S. Q.Wang and H. Q. Ye, First-principles study on elastic properties and phase stability of III-V compounds, Physica status solidi (b) **240** (2003) 45, https://doi.org/10.1002/pssb.200301861

44. W. Voigt, Lehrbuch der Kristallphysik (Textbook of crystal physics) (BG Teubner, Leipzig und Berlin, 1928), https://archive.org/details/bub_gb_SvPPAAAAMAAJ

45. V. Kanchana, G. Vaitheeswaran, and A. Svane, Calculated structural, elastic and electronic properties of SrCl2, Journal of Alloys and Compounds **455** (2008) 480, https://doi.org/10.1016/j.jallcom.2007.01.163

46. R. Terki *et al*., Full potential calculation of structural, elastic and electronic properties of BaZrO3 and SrZrO3, Physica status solidi (b) **242** (2005) 1054, https://doi.org/10.1002/pssb.200402142

47. G. V. Sin'Ko and N. A. Smirnov, Ab initio calculations of elastic constants and thermodynamic properties of bcc, fcc, and hcp Al crystals under pressure, Journal of Physics: Condensed Matter **14** (2002) 6989, https://iopscience.iop.org/article/10.1088/0953-8984/14/29/301/meta

48. M. J. Mehl, B. M. Klein, and D. A. Papaconstantopoulos, First-principles calculation of elastic properties, Intermetallic Compounds **1** (1994) 195, https://apps.dtic.mil/sti/html/trecms/AD1120903/

49. S. F. Pugh, XCII. Relations between the elastic moduli and the plastic properties of polycrystalline pure metals, The London, Edinburgh, and Dublin Philosophical Magazine and Journal of Science **45** (1954) 823, https://doi.org/10.1080/14786440808520496.

50. D. G. Pettifor and O. L. Anderson, Theoretical predictions of structure and related properties of intermetallics, Materials Science and Technology / J. Phys. Chem. Solids 8.4 / **24** (1992 / 1963) 345, https://doi.org/10.1179/mst.1992.8.4.345

51. E. Schreiber, O. L. Anderson, and N. Soga, Elastic Constants and Their Measurements (McGraw Hill, New York, 1973), https://doi.org/10.1115/1.3423687.

52. B. Fultz, Vibrational thermodynamics of materials, Progress in Materials Science **55** (2010) 247, https://doi.org/10.1016/j.pmatsci.2009.05.002.

53. I. Galanakis, Slater-Pauling Behavior in Half-Metallic Heusler Compounds, Nanomaterials **13** (2023) 2010, https://doi.org/10.3390/nano13132010